



# Achieving excellent mechanical properties and wear resistance in Fe<sub>49</sub>Mn<sub>30</sub>Co<sub>10</sub>Cr<sub>10</sub>C<sub>1</sub> interstitial high-entropy alloy via tuning composition and stacking fault energy by Nb doping

Qi Wang, Yanjun Zhou, Xiangtao Deng <sup>\*</sup>, Zhaodong Wang <sup>\*\*</sup>

State Key Laboratory of Rolling and Automation, Northeastern University, 110819, Shenyang, PR China

## ARTICLE INFO

**Keywords:**  
Nb-doped  
High-entropy alloy  
Mechanical properties  
wear

## ABSTRACT

In this study, the effects of Nb doping on the mechanical properties, deformation mechanism, and wear resistance of an Fe<sub>49</sub>Mn<sub>30</sub>Co<sub>10</sub>Cr<sub>10</sub>C<sub>1</sub> interstitial high-entropy alloy (HEA) were studied. Adding 1 at.% Nb resulted in multi-scale NbC particles. The yield strength and elongation remained almost unchanged, and the wear rate was significantly reduced. The precipitation strengthening of nano-NbC particles offsets the decrease in interstitial strengthening. The formation of NbC particles consumed C, reduced the stacking fault energy (SFE) of the alloy, significantly enhanced the transformation-induced plasticity (TRIP) effect, and offsets the deterioration effect of micron-sized NbC particles on plasticity. After adding Nb element, the volume fraction of strain-induced martensitic transformation in the tensile fracture increases from 13.2 % to 30.6 %. The wear mechanism of the two alloys under sliding wear conditions is mainly abrasive wear. Micron-sized NbC blocks the expansion of the groove and protects the matrix. In addition, the Nb-doped high-entropy alloy produced a thicker deformation ultrafine grain layer and a strain-induced phase transition layer below the wear track. The thicker deformation layer and micron-sized NbC particles reduced the wear rate by more than 23.1 %. The rationality of the existing method for calculating the wear rate with the unit load as a parameter was analyzed, and a new method with the unit maximum shear stress as a parameter is proposed.

## 1. Introduction

With the rapid development of aerospace, metallurgy, chemical, nuclear energy, and other industries, stricter requirements have been put forward for high-performance materials. Good comprehensive performance is the key factor in ensuring reliable operation of the system and improving the service life [1,2]. Traditional materials for engineering applications contain one or two main elements, and their comprehensive performance is enhanced by adding a small amount of other elements. However, this material design strategy significantly limits the scope of research and the utilization of materials [3–5]. Compared to traditional materials, high-entropy alloys (HEAs) have more than three main elements, which provides more space for the development of new high-performance materials, and the different terms such as multi-component alloys (MCAs), multi-principal element alloys (MPEAs) and complex concentrated alloys (CCAs) have been used by several researchers. Many HEAs have good wear resistance, corrosion

resistance, and high-temperature properties, and their good overall performance indicates that HEAs have great potential as structural or functional materials [6,7]. However, its high cost and unbalanced performance seriously limit its development and applications. For example, HEAs based on the face-centered cubic (FCC) phase have good room-temperature and low-temperature toughness, but their strength and wear resistance are poor. HEAs based on the body-centered cubic (BCC) phase have high strength but poor toughness.

The metastable HEA Fe<sub>50</sub>Mn<sub>30</sub>Co<sub>10</sub>Cr<sub>10</sub> is a widely studied alloy because of its low cost, good ductility, and plasticity. However, it still has the disadvantages of low strength and hardness, which has stimulated more research on how to improve its mechanical properties [8,9]. The comprehensive mechanical properties can be improved by adding a high-hardness reinforced phase, which is also beneficial for improving wear resistance [10,11]. In order to investigate the potential engineering applications of HEAs, their friction and wear performances have also attracted a wide research interest. Structural materials in the use process

\* Corresponding author.

\*\* Corresponding author.

E-mail addresses: [dengxt@mail.neu.edu.cn](mailto:dengxt@mail.neu.edu.cn) (X. Deng), [zhdwang@mail.neu.edu.cn](mailto:zhdwang@mail.neu.edu.cn) (Z. Wang).

inevitably require the material to have good wear properties; therefore, the development of HEA materials with high strength, good toughness, and excellent wear resistance has broad prospects. Generally speaking, there are two ways to introduce high-hardness reinforcing phases into materials: directly adding reinforcing phases [12] or generating reinforced phases *in situ* through reactions between elements [13]. Compared with the direct addition of the reinforced phase, the *in situ*-generated reinforced phase was clean and pollution-free. A clean interface can significantly improve the mechanical properties of a material. In addition, the *in situ*-generated reinforced phase was small and evenly distributed.

Carbide has high hardness, good high-temperature performance, and chemical stability, making it the preferred material for the reinforcing phase. TiC was a common reinforcing phase with low density, but a large number of literatures show that when the volume fraction was more than 5 %, the ductility will be seriously deteriorated [14]. In our previous study of martensitic wear-resistant steel, TiC particles with a volume fraction of about 1.2 % can be introduced by smelting and continuous casting [3]. When the volume fraction of TiC particles continues to increase, TiC will agglomerate and float due to the density difference between TiC and molten steel, which seriously deteriorates the elongation and toughness, and reduces the yield of Ti element, resulting in a waste of resources. In order to introduce particles with higher volume fraction into the material, NbC particles with a density (7.81 g/cm<sup>3</sup>) similar to that of a metastable HEA matrix [15] are selected to reduce the tendency of particle agglomeration and floating due to density difference during solidification. The addition of NbC to AlCoCrFeNi and Fe<sub>50</sub>Mn<sub>30</sub>Co<sub>10</sub>Cr<sub>10</sub> high entropy alloy coatings can help them obtain higher strengths and good wear resistance [16,17]; additionally, because of the pinning effect of NbC, the high temperature performance of the material can be improved [18]. As reversible hydrogen traps, nano-NbC particles prevent the aggregation of hydrogen at dislocations and significantly improve the resistance to hydrogen embrittlement [19]. Although a large number of research results have proven that the addition of a NbC-reinforced phase is beneficial to the improvement of the comprehensive performance of high-entropy alloys, there are still many uncertainties in the mechanism of its influence on mechanical properties. Additionally, the majority of the research is in the field of coating, with only a few studies on bulk metastable HEAs, and the effect of higher volume particles on mechanical properties and wear resistance needs to be further studied.

In this study, Fe<sub>49</sub>Mn<sub>30</sub>Co<sub>10</sub>Cr<sub>10</sub>C<sub>1</sub> and Nb-doped Fe<sub>48</sub>Mn<sub>30</sub>Co<sub>10</sub>Cr<sub>10</sub>Nb<sub>1</sub>C<sub>1</sub> HEA casting blanks were obtained by conventional vacuum induction furnace melting. After hot and cold rolling, an equiaxed fine grain structure was obtained after annealing at 800 °C for 15 min. The effects of Nb addition on the microstructure, mechanical properties, wear resistance, and deformation mechanism of the Fe<sub>49</sub>Mn<sub>30</sub>Co<sub>10</sub>Cr<sub>10</sub>C<sub>1</sub> alloy were investigated.

## 2. Experimental materials and methods

The Fe<sub>49</sub>Mn<sub>30</sub>Co<sub>10</sub>Cr<sub>10</sub>C<sub>1</sub> (C-HEA) interstitial high-entropy alloy and Fe<sub>48</sub>Mn<sub>30</sub>Co<sub>10</sub>Cr<sub>10</sub>Nb<sub>1</sub>C<sub>1</sub> (NbC-HEA) Nb-doped interstitial high-entropy alloy casting blanks were obtained by melting in an Ar-protected conventional vacuum induction furnace. Metals with a purity of more than 99.9 wt% purchased from Kairui New Material Technology Co., Ltd. (Beijing) were used as raw materials, and the raw materials were dried at low temperature before melting. The casting blanks were forged at 1200 °C to obtain a billet with a cross-sectional size of 100 mm × 100 mm. The billet was heated to 1200 °C, held for 2 h, hot-rolled to 4 mm at 1100 °C, and then cooled to room temperature. The hot-rolled alloy was cold-rolled into a plate with a final thickness of 2 mm and then annealed at 800 °C for 15 min.

The dog-bone standard tensile sample was cut along the rolling direction on an annealed HEA plate. The thickness, width, and length of the gauge section of the samples were 1.6, 12.5, and 25 mm,

respectively. The tensile samples were mechanically polished to remove the oxide layer and macroscopic defects. A tensile test machine was used at room temperature, and the tensile rate was 1 mm/min. On the annealed HEA, a full-thickness sample with dimensions of 12 mm × 20 mm was cut along the rolling direction. The sample was cold-inserted and sealed with epoxy resin to make its 12 mm × 20 mm test surface leak. The epoxy resin AB glue is composed of liquid bisphenol A epoxy resin and liquid polyamide resin. The compressive strength after solidification is above 50 kg/mm<sup>2</sup>, and the shear strength is above 13 kg/mm<sup>2</sup>, which will not affect the test results during the wear process. All the test surfaces of the samples were ground and mechanically polished to a mirror. The wear properties of the two HEAs at room temperature were tested using a ball-on-plate type wear tester (Rete MFT-5000), as shown in Fig. 1. The grinding ball adopted was a 6.35 mm WC ball. WC has a high hardness and elastic modulus, as well as good wear resistance. This ensures that the surface profile of the WC ball changes less during sliding friction and wear, and ensures that a higher contact stress is obtained. In addition, the high hardness difference between the WC ball and the HEA and the good high-temperature stability of WC can reduce the influence of material adhesion on the wear surface of the HEA on the deformation process of the contact surface. The normal loads were 10 N, 20 N, and 30 N. The constant wear rate was 5 mm/s, reciprocating stroke was 5 mm, direction was parallel to the rolling direction, and test time was 60 min. The rationality of the experimental parameter selection is discussed in the discussion section. At the end of the test, the wear traces of the cleaned debris were characterized using a white-light interference three-dimensional topography instrument on the test machine. To obtain more reliable experimental results, each material was subjected to three wear experiments, and the average value was considered the accurate wear rate.

The tensile fracture and wear morphologies were characterized using a Zeiss crossbeam550 focused ion beam scanning electron microscope (FIB-SEM) to analyze the fracture and wear mechanisms. The phase composition and microstructure of the annealed sample, fracture cross-section sample, and wear trace cross-section sample were characterized by an Oxford symmetry electron backscatter diffraction (EBSD) probe equipped with a SEM. The EBSD operating voltage was 20 kV, and the step size was 50 nm. Channel 5 and the AZtecCrystal software were used to post-process the data. The stress layer of the sample used in the EBSD was removed by electrolytic polishing. The microstructure of the annealed samples was characterized by transmission electron microscopy (TEM) on a TECHNAIG2 F20 instrument produced by FEI

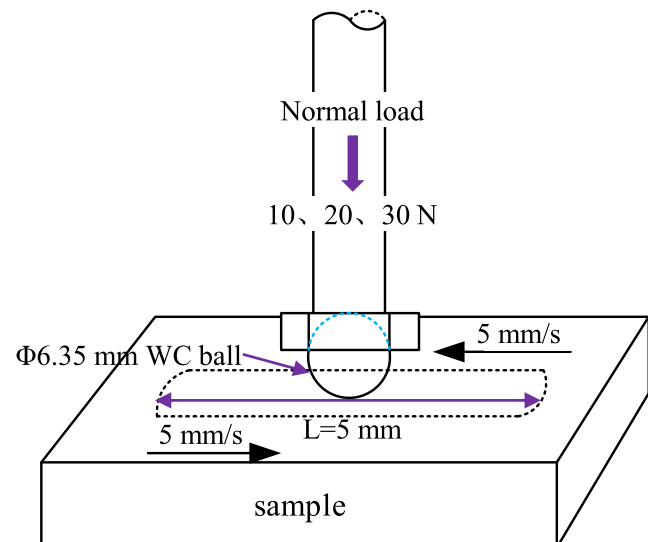


Fig. 1. Diagram of wear test.

Company in the United States. The operating voltage was 200 kV. The morphology and crystal structure of the matrix and precipitated phase were analyzed using selected-area diffraction and energy spectra.

### 3. Experimental results and discussion

#### 3.1. Analysis of microstructure and mechanical properties of annealed alloy

**Fig. 2** shows the microstructures of the two alloys after annealing. The inverse pole figure (IPF) map of the C-HEA sample after annealing shows that the grains are equiaxed. At the same time, the grain size was not uniform, and there were large abnormal grains. The TEM results showed that there were a large number of recrystallized grains without dislocation density in the C-HEA sample. During the recrystallization process, annealing twins were formed, and a small amount of precipitate was observed. The IPF map of the annealed NbC-HEA sample showed that the grains were uniformly distributed, equiaxed, and of uniform size, with no abnormal grains of large sizes found. A large number of

recrystallized grains and annealing twins without dislocation density were also observed in the TEM image, along with many nanoscale precipitates. The composition analysis of the precipitates showed that they were rich in Nb. The results of selective diffraction analysis showed that the precipitates had a FCC structure, indicating that the precipitates were NbC. The nano-precipitation of NbC can play a role in precipitation strengthening and improve the strength of NbC-HEA sample. In addition, a large number of micron- and submicron-sized NbC particles with a volume fraction of about 2.3 % were observed (**Fig. 2d**). The micron- and submicron-sized NbC particles play the role of particle strengthening, and have little contribution to the strength. The main role is to improve the wear resistance, which is the same as the hard particles in metals and composites. NbC can pin the grain boundaries, refine the grains, and prevent abnormal grain growth [20]. Therefore, no large abnormal grains were observed in the NbC-HEA sample.

Statistical analysis of the grain sizes of the two alloys showed that the grain size distribution of the NbC-HEA sample was more concentrated, while the grain size distribution of the C-HEA sample was more dispersed. The proportion of grains with a size of less than 1  $\mu\text{m}$  in the C-

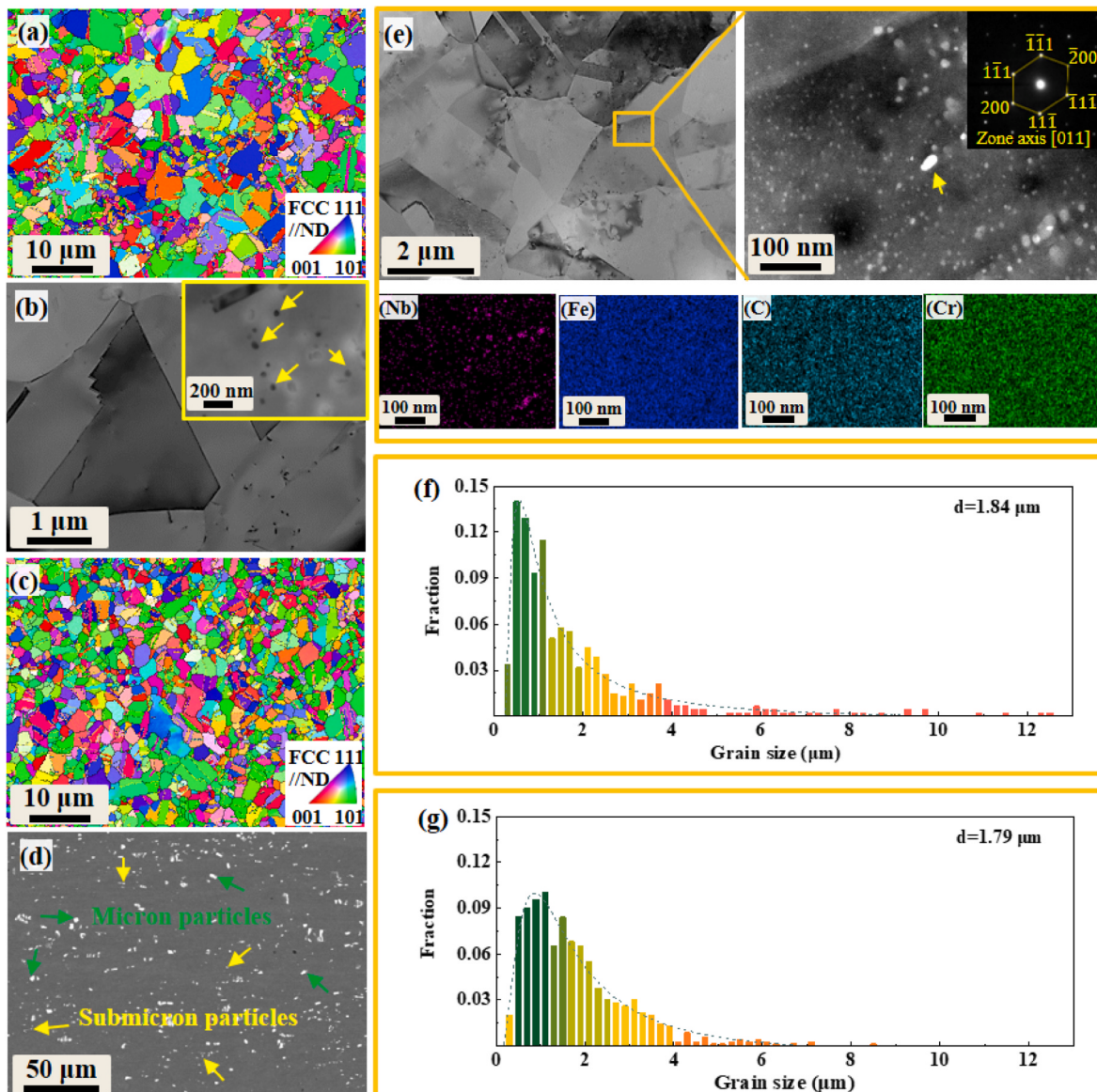


**Fig. 2.** The microstructure of annealed samples: (a) IPF map of C-HEA sample; (b) TEM image of C-HEA sample; (c) IPF map of NbC-HEA sample; (d) The particle morphology of NbC-HEA sample; (e) TEM image of nano-precipitation and corresponding element distribution of NbC-HEA sample; (f) Grain size distribution of C-HEA sample; (g) Grain size distribution of NbC-HEA sample.

HEA sample was 0.39, and there were large grains with a size of more than 10  $\mu\text{m}$ ; the proportion of grains smaller than 1  $\mu\text{m}$  in the NbC-HEA sample was only 0.28, and most of the grains were smaller than 4  $\mu\text{m}$ . Although the grain size distributions of the two alloys were different, their average grain sizes were similar, at approximately 1.8  $\mu\text{m}$ .

After the annealing heat treatment, the yield strengths of the two alloys were similar at 549 and 547 MPa, respectively, but the tensile strengths were different. The tensile strength of the C-HEA sample was 995 MPa, whereas that of the NbC-HEA sample was 937 MPa (Fig. 3). As shown in Fig. 2, numerous NbC particles are observed in the NbC-HEA sample. The formation of NbC particles consumes a large amount of C element. The C element is a common interstitial solid solution element, and the decrease in the mass fraction of solid solution C reduces the solid solution strengthening effect and yield strength. However, the NbC particles produced precipitation strengthening, and the synergistic effect of the two strengthening mechanism made the yield strengths of the two alloys similar. The addition of a large number of carbides or oxides in high-entropy alloys will result in a significant reduction in elongation [21,22], but the elongation of the NbC-HEA sample was slightly lower than that of the C-HEA sample, from 48.9 % to 47.6 %.

Fig. 4 shows the tensile fracture morphology of the two alloys. According to the macroscopic fracture morphology, the local necking did not appear in the C-HEA sample, but it appeared in the NbC-HEA sample in the middle of the width. The local amplification of the tensile fracture morphology shows that the two alloys were characterized by dimples and tearing ridges, and the size of the dimples in the C-HEA sample was relatively uniform. Many large size dimples were observed in NbC-HEA sample, and the existence of particles was detected in the large size dimples. The composition analysis of the particles shows that they were NbC particles.

To analyze the mechanism of tensile fracture of the NbC-HEA sample and the effect of NbC particles on crack initiation and propagation, the particles near the tensile fracture of the NbC-HEA samples were characterized, as shown in Fig. 5. After tensile deformation, a large number of NbC particles fractured. At the same time, because the deformation abilities of the particles and the matrix were different, a small number of particles and the matrix were debonded, and micro-holes were formed between the particles and the matrix along the tensile direction; however, no cracks formed by micro-hole aggregation were observed. In addition, the existence of large dimples in the tensile fracture morphology indicated that the material underwent a large plastic deformation before fracture, indicating that the material has a strong ability to resist crack propagation [23]. Although the NbC particles were fractured during the deformation process and the particles and matrix

were debonded to form micro-voids, the material still underwent large plastic deformation before the micro-voids aggregated and grew, which reduced the deterioration of the tensile plasticity of the NbC particles. Comparing Fig. 4b and c, large-sized particles above 5  $\mu\text{m}$  were easily fractured during deformation, whereas small-sized particles below 2  $\mu\text{m}$  were basically not fractured. In addition, the existence of secondary cracks can be observed in Fig. 5d, but no particles were observed near the cracks, indirectly indicating that the particles were not the only weak area in the tensile fracture.

Particles were only one of the factors that affect the mechanical properties of the alloy. EBSD analysis of tensile fracture can be used to analyze the deformation mechanism of the alloy during the tensile process. Fig. 6 shows the EBSD analysis results of the tensile fractures of the two alloys. According to Fig. 6a1 and a2, the deformation mechanisms of the two alloys were the same, but only a small amount of hexagonal close packed (HCP) martensite was observed in the tensile fracture of the C-HEA sample, and the volume fraction was approximately 13.2 %. The tensile fracture of NbC-HEA sample revealed more HCP martensite, with a volume fraction of approximately 30.6 %. Because Nb doping consumes an equal atomic ratio of C, the stacking fault energy (SFE) of NbC-HEA was lower than that of C-HEA [24,25]. The simulation result of stacking fault energy of C-HEA by JMatPro software is 36.0 J, and that of NbC-HEA is 29.8 J. The lower stacking fault energy promoted the generation of the HCP phase, improved the work hardening ability through the transformation-induced plasticity (TRIP) effect, delayed the generation of the necking phenomenon, and improved the elongation [26,27]. The kernel average misorientation (KAM) map showed that the dislocation densities of the two alloys after deformation were not significantly different.

According to the IPF, the grains rotated after deformation, forming a texture with a certain intensity. An orientation distribution function (ODF) map was used to analyze the texture evolution of the tensile fracture, as shown in Fig. 7. The maximum texture intensity of the C-HEA sample was 10.67, with obvious copper (90, 35, 45) and S (59, 37, 63) textures, and weak A (35, 90, 45) textures. The volume fractions of the copper, S, and A textures were 24.8 %, 14.1 %, and 2.8 %, respectively. In contrast, the maximum texture intensity of the NbC-HEA sample was slightly reduced to 6.67, and it also had obvious copper and S textures; however, the texture intensity of the A texture increased. The volume fractions of the copper, S, and A textures were 15.8 %, 14.2 %, and 5.2 %, respectively. The copper texture is a typical tensile texture. The grain deformation got more severe as the volume percentage of copper texture increased, and the direction of most grains eventually turned parallel to the tensile direction. Comparing the texture changes of the tensile fractures of the two alloys, the C-HEA sample had a higher volume fraction of the copper texture than the NbC-HEA sample. The main reason for this was that the NbC in the NbC-HEA sample had a pinning effect on the dislocations and grain boundaries.

According to the Schmid factor distribution map of the microstructure near the tensile fracture structure (Fig. 8), there were more grains with a low Schmid factor in the microstructure near the tensile fracture structure of the C-HEA sample, which is also consistent with the results of the texture analysis. Because of the high-volume fraction of copper texture in the tensile fracture structure of the C-HEA sample, the direction of the copper texture grains was parallel to the tensile direction, resulting in a decrease in the Schmid factor. In the case of constant shear stress, a lower Schmid factor leads to an increase in the external stress of the initiation slip, which was one of the reasons for the higher tensile strength of the C-HEA samples [28,29].

### 3.2. Wear results analysis and discussion

The friction coefficient of the alloy during wear can be obtained from the real-time friction and positive pressure data collected by the wear tester. In general, based on the change in the friction coefficient in the wear process, it can be divided into four stages, namely, the running-in

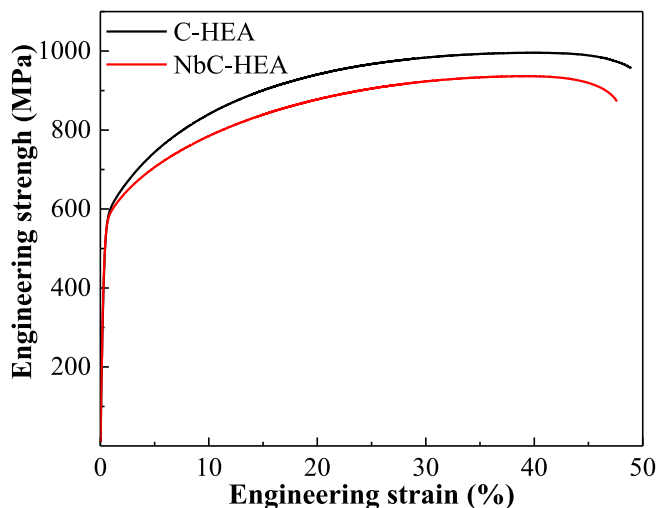
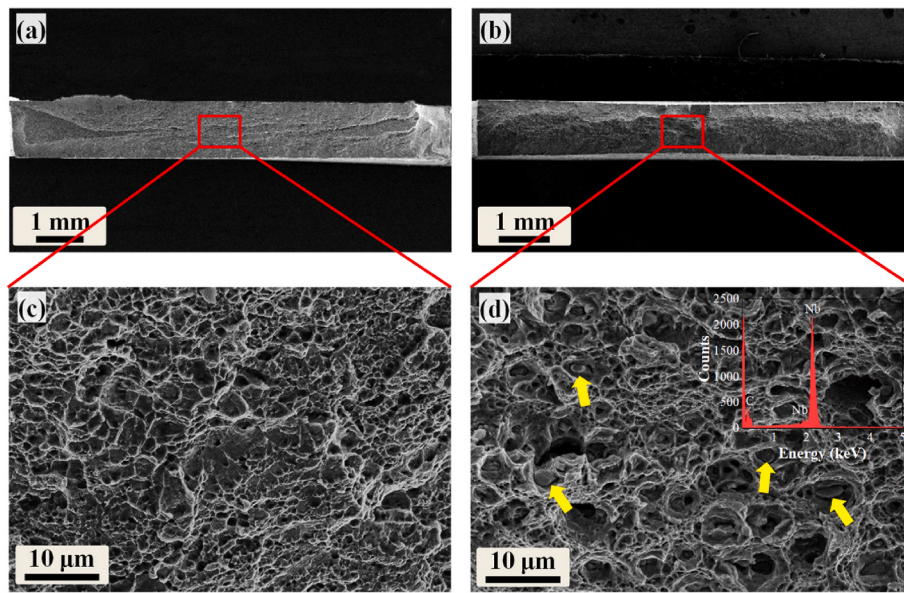
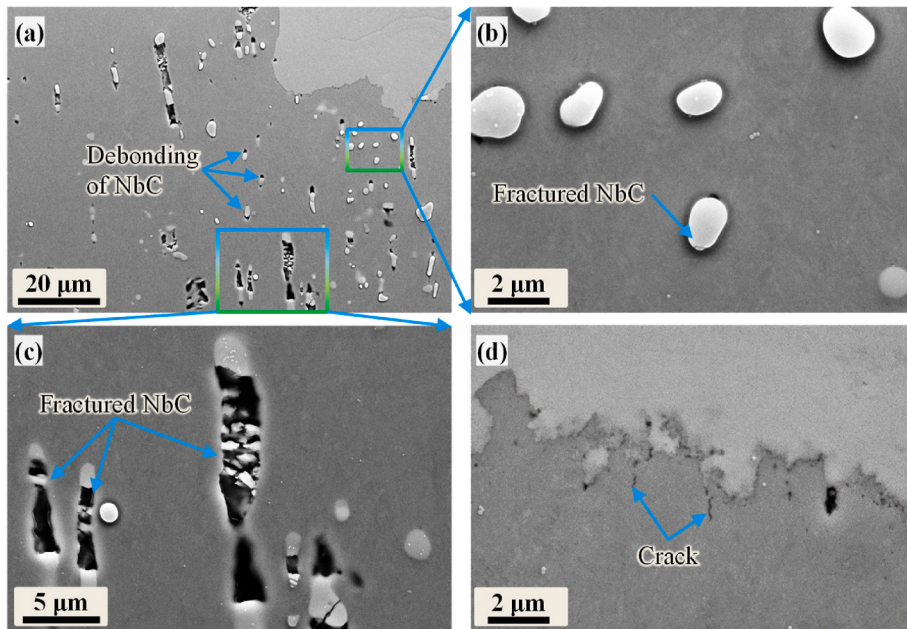


Fig. 3. Tensile curves of annealed samples.



**Fig. 4.** The tensile fracture morphology of the two alloys: (a) and (c) C-HEA sample; (b) and (d) NbC-HEA sample.



**Fig. 5.** Particle morphology near the tensile fracture of the NbC-HEA sample.

period, the stable period after running-in, the falling period, and the low stable period [30]. However, under the experimental conditions used in this study, the friction coefficients of the two alloys did not appear in these four stages, and there was only one stable period and no obvious running-in period (Fig. 9). This may be because the alloy did not form a stable glaze layer and the friction coefficient did not decrease. In addition, the friction coefficient fluctuated significantly, particularly at lower loads. In addition, the friction coefficients of the NbC-HEA samples were slightly larger than those of the C-HEA samples. When the loads were 10, 20, and 30 N, the average friction coefficients of C-HEA samples were 0.29, 0.28, and 0.28, respectively, and the average friction coefficients of NbC-HEA samples were 0.31, 0.30, and 0.29, respectively. The micron and submicron NbC particles with high hardness in the NbC-HEA sample hindered the movement of the grinding ball during the wear process. This was why the average friction coefficient of the

NbC-HEA sample increased slightly.

The 3D morphology of the wear tracks of the two alloys was characterized using a white light interferometer on the wear tester, and the cross-sectional profile was analyzed. The 2D cross-sectional profile after wear is shown in Fig. 10. The wear track depth of the NbC-HEA sample was significantly smaller than that of the C-HEA sample, and the wear track depth of the two alloys increased with increasing load. The literature shows that the friction coefficient is related to roughness, and increasing roughness leads to an increase in the friction coefficient and friction coefficient volatility [31]. As shown in Fig. 10, the cross-sectional profile of the wear track was serrated. With an increase in load, the serration phenomenon gradually weakened, indicating that the roughness of the wear track surface decreased. This phenomenon can explain the change in the friction coefficient.

The wear volumes of the two alloys under different loads were ob-

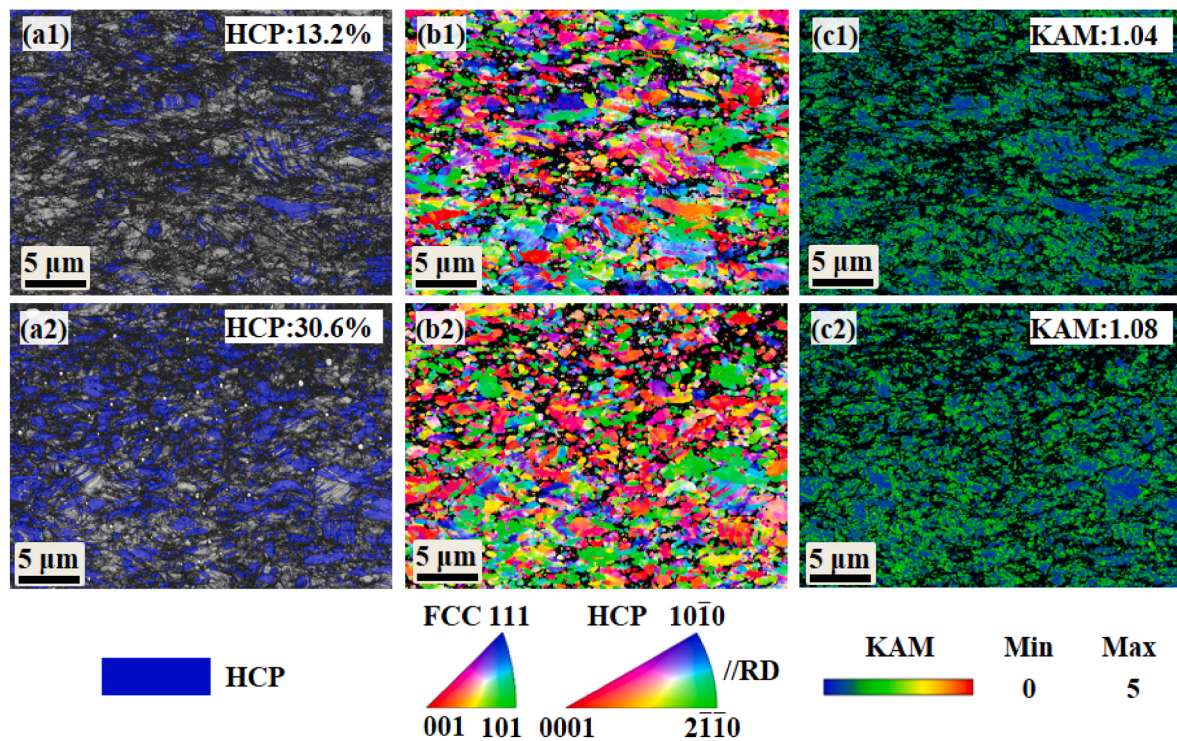


**Fig. 6.** EBSD analysis results of the microstructure near the tensile fracture of two alloys: (a) HCP phase distribution; (b) IPF map; (c) KAM map; (1) C-HEA sample; (2) NbC-HEA samples.

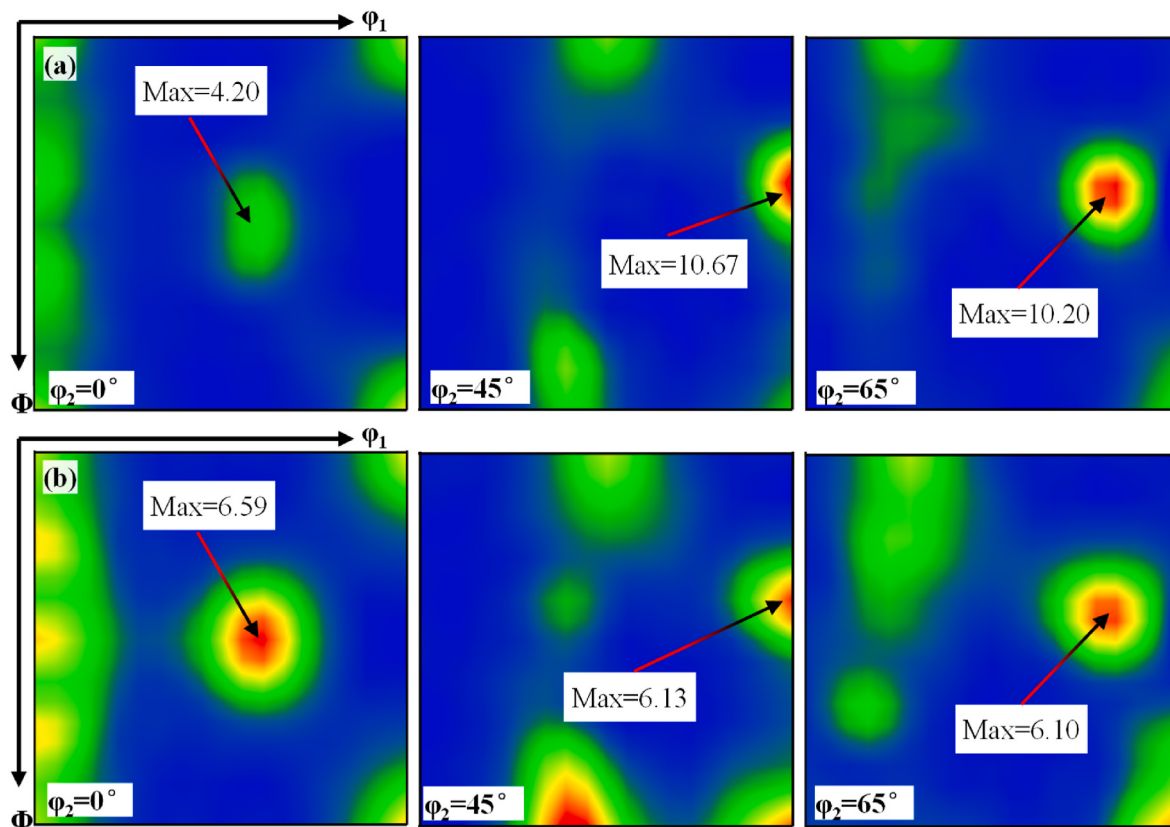


**Fig. 7.** ODF map of the microstructure near the tensile fracture of two alloys: (a) C-HEA sample; (b) NbC-HEA samples.

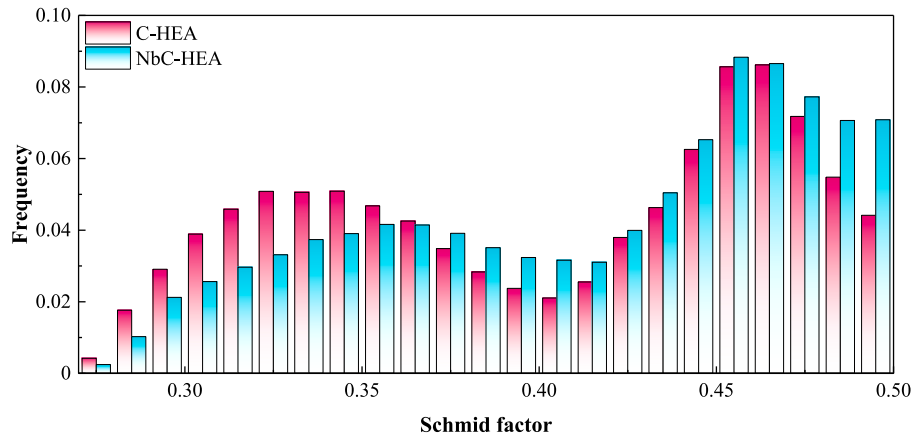


**Fig. 8.** Schmid factor distribution map of tensile fracture microstructure of two alloys.

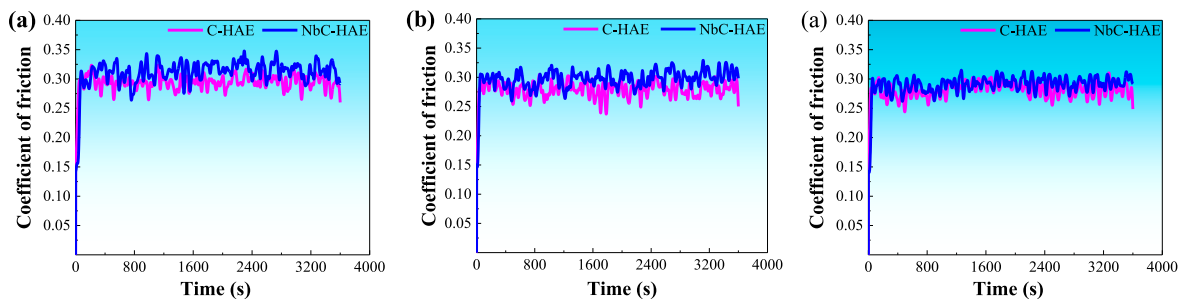


**Fig. 9.** The friction coefficients of the two alloys under different loads: (a) 10 N; (b) 20 N; (c) 30 N.

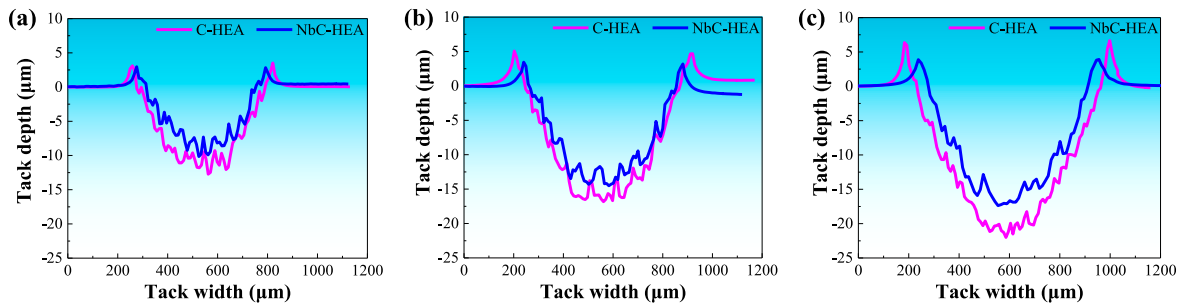


**Fig. 10.** The 2D cross-section profiles of the two alloys under different load wear: (a) 10 N; (b) 20 N; (c) 30 N.

tained using a white-light interferometer, and the wear rate was calculated according to Eq. (1) [32]:

$$\omega = \frac{V_{\text{loss}}}{P \times L} \quad (1)$$

where  $\omega$  is the wear rate,  $\text{mm}^3/(\text{N}\cdot\text{m})$ ;  $V_{\text{loss}}$  is the wear volume,  $\text{mm}^3$ ;  $P$  is the load, N;  $L$  is the wear length, m.

According to the calculation results, the wear rate of the NbC-HEA sample was lower than that of the C-HEA sample, and the wear rate decreased with an increase in the load (Fig. 11). When the loads were 10, 20, and 30 N, the wear rates of NbC-HEA samples were  $7.73 (\pm 0.22)$ ,  $7.07 (\pm 0.14)$ , and  $6.75 (\pm 0.18) \times 10^{-5} \text{ mm}^3/(\text{N}\cdot\text{m})$ , respectively, while the wear rates of C-HEA samples were  $10.67 (\pm 0.19)$ ,  $9.67 (\pm 0.24)$  and  $8.78 (\pm 0.30) \times 10^{-5} \text{ mm}^3/(\text{N}\cdot\text{m})$ , respectively. This result is similar to the wear rate of HEAs reported by early researchers [11,33,34]. When the loads were 10, 20, and 30 N, the wear rates of NbC-HEA samples decreased by 27.6 %, 26.9 %, and 23.1 %, respectively, compared with C-HEA samples.

Wear is a complex stress process, and the material is subjected to the combined action of positive pressure and frictional shear stress; therefore, only considering the influence of load on the wear rate is not comprehensive. The physical properties of the two materials also had a significant impact on the wear rate of the material. The positive pressure and friction shear stress of the material under different loads were calculated theoretically. According to the Hertz contact theory [35], the contact radii of the WC ball and HEA after applying stress can be calculated using Eq. (2).

$$a = \left( \frac{3PR}{4E^*} \right)^{\frac{1}{3}} \quad (2)$$

where  $P$  is the positive pressure, N;  $R$  is the equivalent radius of curvature, m;  $E^*$  is the effective elastic modulus, Pa. Additionally,

$$\frac{1}{R} = \frac{1}{R_1} + \frac{1}{R_2} \quad (3)$$

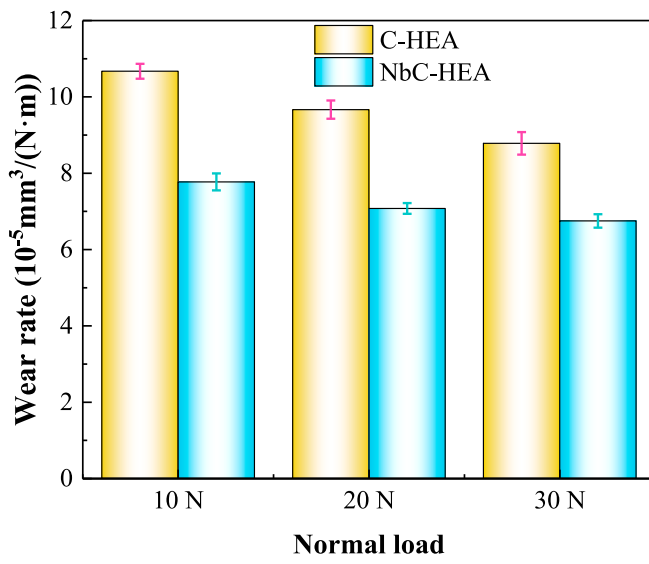


**Fig. 11.** Wear rates of two alloys under different loads.

$$\frac{1}{E^*} = \frac{1 - \nu_1^2}{E_1} + \frac{1 - \nu_2^2}{E_2} \quad (4)$$

where  $R_1, E_1, \nu_1$  and  $R_2, E_2, \nu_2$  are the curvature radius, elastic modulus, and Poisson ratio of the WC ball and HEA, respectively. The HEA is a rectangular sample, and the radius of curvature is infinite. According to the above equation, when the positive pressures are 30, 20, and 10 N, the contact radii are 0.074, 0.065, and 0.051 mm, respectively.

The maximum stress  $p_{\max}$  of the Hertz contact zone between the WC ball and HEA is 1.5 times the average stress  $p_0$ , that is,

$$p_{\max} = \frac{3}{2} p_0 = \frac{3P}{2\pi a^2} \quad (5)$$

When the loads were 10, 20, and 30 N, the maximum stresses were 1.80, 2.27, and 2.60 GPa, respectively. The maximum stress was much larger than the yield strength, but the maximum normal stress did not increase linearly with an increase in the load. When the applied stress is greater than the yield strength of the material, it undergoes significant wear. According to the above equations, the higher the elastic modulus of the grinding ball, the smaller the contact radius, the higher the contact stress. The commonly used grinding balls are Si<sub>3</sub>N<sub>4</sub>, Al<sub>2</sub>O<sub>3</sub>, GCr15, WC and SiC with elastic modulus of 320, 420, 208, 680 and 410 GPa, respectively. WC has the highest elastic modulus, which is beneficial to obtain higher contact stress. The high contact stress can simulate the wear in harsh environments, accelerate the wear process, and more easily reflect the difference in wear resistance. The second invariant of the stress tensor in the von Mises yield criterion can accurately determine whether the material has shear yield or not.

Without considering friction, the stress distribution in the Hertz contact area between the WC ball and HEA can be calculated as follows:

$$p(r) = p_{\max} (a^2 - r^2)^{1/2} \quad (6)$$

where  $r$  is the distance between any point on the contact area and the contact center point, m.

Considering friction, the stress distribution in the Hertz contact zone between the WC ball and HEA can be calculated as follows:

$$p(r) = \mu p_{\max} (a^2 - r^2)^{1/2} \quad (7)$$

where  $\mu$  is the friction coefficient.

According to Hamilton's work [36,37] on the stress field during wear, the stress components and second invariant of the stress tensor in

the von Mises yield criterion can be calculated as follows:

$$\begin{aligned} \sigma_x = \sigma_y &= p_{\max} \left\{ (1 + \nu) \left[ \zeta \arctan \left( \frac{1}{\zeta} \right) - 1 \right] + \frac{1}{2(1 + \zeta^2)} \right\} \\ \sigma_z &= -p_{\max} \frac{1}{(1 + \zeta^2)} \\ \tau_{zx} &= \mu p_{\max} \left[ -1 + \frac{3}{2} \zeta \arctan \left( \frac{1}{\zeta} \right) - \frac{\zeta^2}{2(1 + \zeta^2)} \right] \\ \tau_{yz} &= \tau_{xy} = 0 \\ J_2 &= \tau_{zx}^2 + \tau_{yz}^2 + \tau_{xy}^2 + \frac{1}{6} [(\sigma_x - \sigma_y)^2 + (\sigma_y - \sigma_z)^2 + (\sigma_z - \sigma_x)^2] \end{aligned} \quad (8)$$

where  $\zeta = \frac{z}{a}$ , and  $z$  is the distance between any point below the contact area and the contact area in the loading direction, m.

$$2\sigma_s^2 = 6K^2 \quad (9)$$

where  $\sigma_s$  is the yield strength of the material, MPa;  $K$  is the shear yield strength of the material. When  $\sqrt{J_2} > K$ , the material undergoes shear yield during wear.

Hamilton [37] provides the relationship between the maximum values of  $\sqrt{J_2}/p_{\max}$  and  $\mu$  in the subsurface and surface by calculation. As shown in Fig. 12, with an increase in the friction coefficient, the maximum shear stress gradually shifts from the subsurface to the surface position. To facilitate the calculation, the friction coefficient was uniformly set at 0.3.

When the loads were 10, 20, and 30 N, the  $\sqrt{J_2}$  can be obtained as 855, 1077, and 1232 MPa, respectively, while the shear yield strengths of the two alloys were 317 and 316 MPa, respectively, indicating that the material has a shear yield during the wear process, and the maximum shear stress was on the surface. According to the above calculation, an increase in load leads to an increase in the contact area, and the normal stress and shear stress do not increase linearly with an increase in load. Therefore, the wear rate calculated according to Equation (1) decreases with an increase in the load. However, the real cause of material wear is stress, not external load; therefore, the existing evaluation method for wear rate is not reasonable. In this study, the maximum normal stress or maximum shear stress, rather than the load, is proposed as a parameter to calculate the wear rate. A proportional relationship exists between the maximum normal stress and the maximum shear stress, and the two are equivalent. Because the

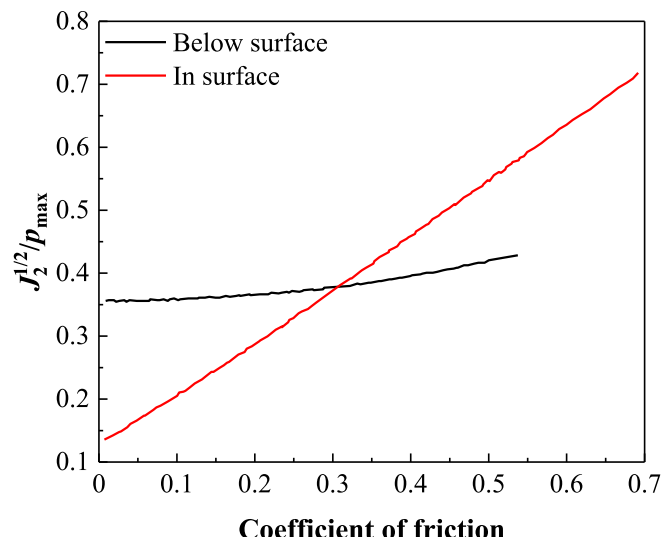


**Fig. 12.** The relationship between the maximum values of  $\sqrt{J_2}/p_{\max}$  and  $\mu$  in the subsurface and surface [37].

maximum shear stress considers the shape and size of the grinding pair, as well as the elastic modulus and Poisson ratio of the two materials, the evaluation method of the wear rate is more objective, and the influence of the physical properties of the material on the wear is excluded. The new wear rate calculation method is expressed in Equation (10).

$$\omega = \frac{V_{\text{loss}}}{\sqrt{J_2} \times L} \quad (10)$$

According to Eq. (10), the wear rates of NbC-HEA samples at loads of 10, 20, and 30 N were  $1.79 (\pm 0.05)$ ,  $2.60 (\pm 0.05)$ , and  $3.25 (\pm 0.08) \times 10^{-6} \text{ mm}^3/(\text{MPa}\cdot\text{m})$ , respectively, while the wear rates of C-HEA samples were  $2.46 (\pm 0.04)$ ,  $3.56 (\pm 0.08)$ , and  $4.23 (\pm 0.14) \times 10^{-6} \text{ mm}^3/(\text{MPa}\cdot\text{m})$ , respectively. The wear rate obtained using the maximum

shear stress was significantly different from that obtained using the load. The wear rate obtained by the new evaluation method gradually increased with an increase in the load.

The wear track morphology at 30 N load was characterized by SEM, as shown in Fig. 13, and the wear mechanism was analyzed. The wear-track width of the C-HEA sample was 738 μm, whereas that of the NbC-HEA sample was 704 μm. For the two alloys with similar hardness and elastic modulus, the larger the wear track width, the deeper the wear track depth, and the more severe the wear, which is consistent with the analysis results of the wear rate. A large number of micro-grooves were observed in the wear morphology of the C-HEA samples, indicating that the wear mechanism was mainly abrasive wear. Simultaneously, a large amount of wear debris with a size of less than 5 μm was found. Through

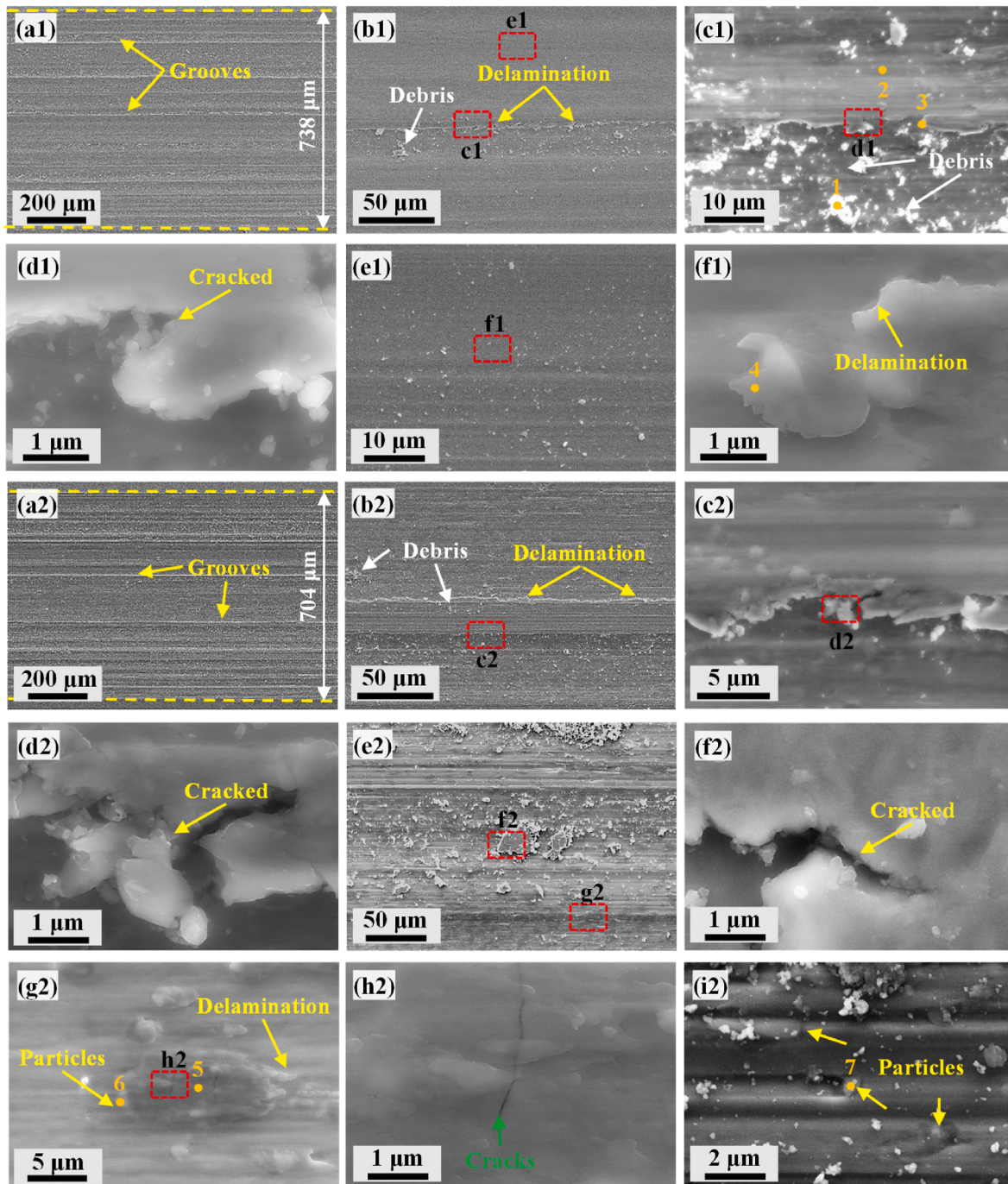


Fig. 13. SEM morphology of the wear tracks at 30 N load of the two alloys: (a) C-HEA sample; (b) NbC-HEA sample.

the locally enlarged wear morphology, wear debris was mainly generated by delamination and spalling of the groove edge with the characteristic of fatigue wear. The crack shown in Fig. 13d1 support this view. Fish-scale-like delamination can be observed in micron-grooves, which was also a form of fatigue spalling (Fig. 13f1). The wear morphology of the NbC-HEA sample was similar to that of the C-HEA sample, and there were more grooves and debris. The large micron debris will gradually break into small debris (Fig. 13f2). The difference was that a large number of oxidized regions were observed in micron-grooves, and the oxidized regions were often distributed around NbC particles (Fig. 13g2). The existence of cracks can be observed by amplifying the oxidation area (Fig. 13h2). The toughness of metal oxides was poor, and crack was more likely to occur after repeated fatigue deformation. The reason why the oxidation area was often distributed around the NbC particles may be related to the hindering effect of the particles on the abrasive, resulting in an increase in the instantaneous friction coefficient and a serious local temperature rise. In addition, it can be seen from the locally enlarged wear morphology that the NbC particles in the NbC-HEA sample can block the grooves (Fig. 13i2), which hinders the removal of the material by the grinding ball and reduces the wear rate.

Table 1 is the EDS analysis results at various positions of the wear tracks at 30 N load in Fig. 13. According to the results, the presence of W element is not detected on the wear tracks of the two alloys, which indicated that the WC ball does not undergo adhesive wear during the wear process, ensuring the stability of the contact radius and contact stress. The debris undergone obvious oxidation (position 1), while the oxidation of matrix was not obvious (position 2). At the edge of micron grooves, the material will also be oxidized after repeated deformation, which will produce cracks and spalling to form wear debris (position 3). However, the fish-scale-like delamination inside the micron grooves of the C-HEA sample was entirely due to fatigue-induced spalling, as no oxidation features were detected in this region (position 4). It is verified by EDS that a large number of oxidized areas (position 5) were observed in the micron grooves of the NbC-HEA sample, and the oxidized areas were often distributed around the NbC particles (position 6). In addition, the EDS analysis results also prove that NbC particles can block the grooves (position 7).

The results of a large number of literatures also shown that the addition of carbides [38], borides [39], oxidases [40] and intermetallic [41] with higher hardness to the matrix can improve the wear resistance. The effect was to increase the hardness of the material or to reduce the friction coefficient. However, hard particles can not only strengthen the matrix, but also improve the wear resistance of micron particles. However, the presence of micron particles will slightly increase the friction coefficient and the fluctuation of the friction coefficient. The hardness of the annealed C-HEA sample and NbC-HEA sample was 292 and 285 HV, and the hardness of the two alloys was similar. Because the formation of NbC will consume a certain amount of interstitial carbon atoms and reduce the effect of solid solution strengthening, but it will produce a large amount of nano-NbC precipitation and improve the effect of precipitation strengthening, finally, the hardness of the two alloys was similar. Therefore, the effect of hardness on wear resistance can be ruled out in the process of wear. It can be considered that the improvement of wear resistance of NbC-HEA samples was entirely due to NbC particles.

**Table 1**

EDS analysis results at various positions of the wear tracks at 30 N load (at.%).

Element	Fe	Mn	Co	Cr	C	Nb	O	W
1	20.89	13.05	4.24	4.29	15.74	0	41.79	0
2	30.99	19.71	6.19	6.36	36.75	0	0	0
3	23.38	15.39	5.10	5.21	22.10	0	28.82	0
4	27.25	19.37	5.64	7.02	40.71	0	0	0
5	19.81	13.94	4.07	4.61	10.01	0	47.57	0
6	14.33	11.31	2.99	4.13	9.51	11.22	45.51	0
7	17.05	11.68	3.67	4.50	50.04	13.06	0	0

Through the observation of the particle morphology of the NbC-HEA sample subsurface after wear, it was found that although the material was subjected to high stress during the wear process, the particles and the matrix still maintained a good interface, and there was no crack between the particles and the matrix due to different strains (Fig. 14a). However, the larger particles have been damaged and cracks have appeared on the particles. The particle damage in Fig. 14b is more obvious and has been split into many small debris particles. At the same time, it also proves that the particles can indeed play a role in protecting the matrix. The groove depth on the left and right sides of the particles was deeper. The particles were exposed to the matrix and protect the matrix below the particles. While the particles were damaged under the repeated impact of the grinding ball.

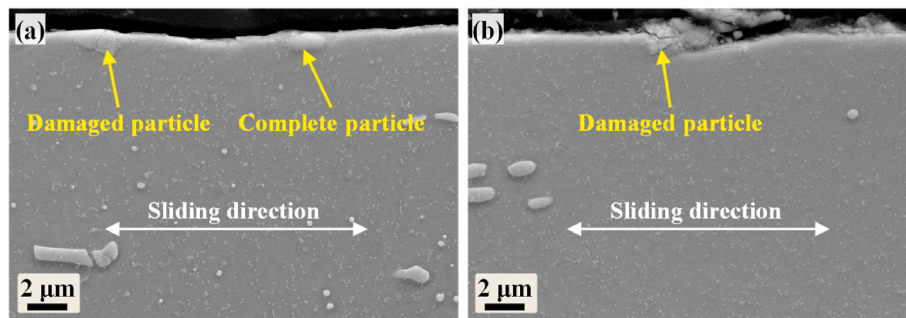
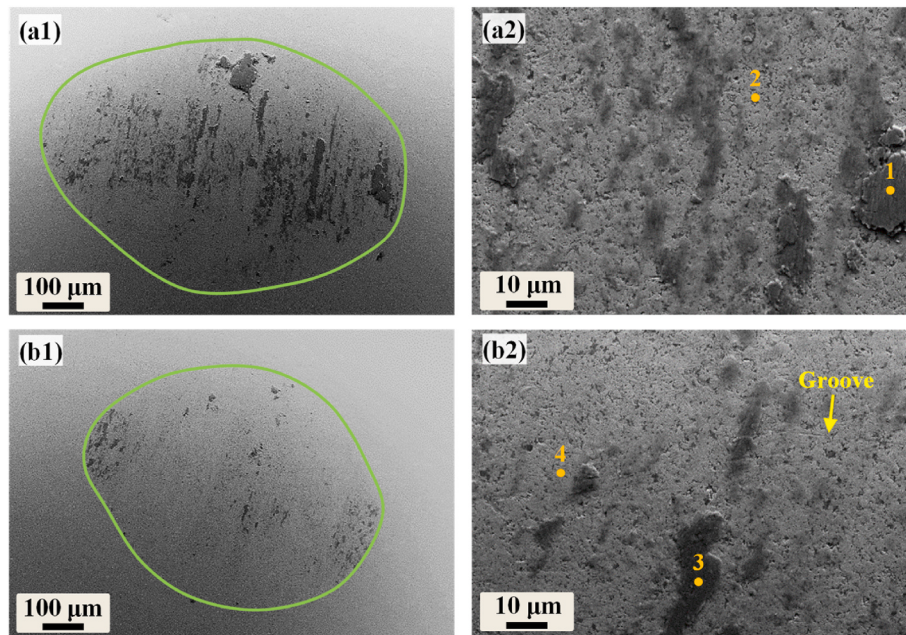
In order to systematically analyze the material transfer during the wear process and prove that the WC ball will not undergo obvious contour changes during the wear process, the wear traces of the WC balls were observed by SEM. After the wear of WC balls with two high-entropy alloys, obvious areas with adhesive wear characteristics were observed, and the contact area between WC balls and C-HEA samples after wear was significantly larger than that between WC balls and NbC-HEA samples after wear, because the wear of C-HEA samples was more serious, resulting in an increase in the contact area. In addition, through local amplification, no obvious wear trace after wear on WC balls was observed, while a small amount of small groove after wear on WC ball against NbC-HEA samples was observed, indicating that both HEA samples were not produced obvious wear on WC balls. Because the hardness of WC balls is much higher than that of HEA samples. In addition, the elastic modulus of WC balls is high, the contact area is small, so no obvious contour change occurs during wear. The composition analysis of the area with obvious adhesion characteristics and the area with no obvious adhesion characteristics on the WC ball was carried out (see Table 2). The results showed that the area with obvious adhesion characteristics was the adhesive HEA material, and the presence of Nb element was detected in the area of Fig. 15b2. But the presence of HEA material was also detected in the area with no obvious adhesion characteristics, indicating that the HEA material had obvious material transfer to the WC balls. In addition, the percentage of oxygen atoms in the region with obvious adhesion characteristics was high, indicating that oxidative wear was presented. The above analysis shown that only the material in the sample transferred to the grinding ball in the form of adhesive wear, and the material in the grinding ball did not transfer to the sample. In addition, according to the analysis of the morphology of the grinding ball, the surface of the grinding ball was smooth and no obvious wear trace. Therefore, it can be determined that the grooves in the wear tracks of the sample were generated by the wear debris of the sample during the wear process under the abrasive wear mechanism, and the sample, the wear debris and the grinding ball produced a three-body wear state.

The deformation mechanism of the alloy during the wear process was analyzed using EBSD of the subsurface structure of the wear track at 30 N load. The worn subsurface is divided into a severe deformation zone, a deformation transition zone, and a matrix [42]. Owing to the interaction of various deformation mechanisms, the severe deformation zone usually leads to the refinement of the structure into nanoscale grains [43]. The TRIP effect occurred in the subsurface of the C-HEA sample after wear, but only a small amount of the HCP phase was produced, and the thickness of the deformation layer with the TRIP effect was small, only 15  $\mu\text{m}$  (Fig. 16a1). In addition, there were more HCP phases near the surface of the wear track, and the shape was blocky. The HCP phase volume fraction far from the surface of the wear track gradually decreased, and the shape gradually became lath-shaped. The generation of the HCP phase and the breakage of grains during wear cause grain refinement, forming a deformed ultrafine-grained layer (DUGL). Fig. 16b1 clearly shows an obvious grain refinement area in the subsurface. According to the statistics of the grain size of the deformed layer structure marked in Fig. 16a1, the grain size of the region can be

**Table 2**

EDS analysis results at various positions of the WC grinding ball at 30 N load (at.%).

Element	Fe	Mn	Co	Cr	C	Nb	O	W
1	24.27	14.59	5.84	4.33	10.32	0	40.65	0
2	3.82	2.24	2.60	0.65	42.81	0	27.59	20.29
3	14.06	8.73	2.91	3.04	21.01	1.57	48.68	0
4	4.81	2.77	2.5	1.04	36.67	0	29.19	22.98

**Fig. 14.** The particle morphology of the NbC-HEA sample subsurface after wear.**Fig. 15.** SEM morphology of the WC grinding ball after wear against the two alloys at 30 N load: (a) C-HEA sample; (b) NbC-HEA sample.

obtained to be 0.74  $\mu\text{m}$ , whereas the grain size of the matrix was 1.84  $\mu\text{m}$ , indicating that wear refined the subsurface grain and produced work hardening. The kernel average misorientation (KAM) distribution map of the subsurface microstructure also showed the existence of a deformed layer; however, the thickness of the KAM value was significantly higher, approximately 1.8  $\mu\text{m}$ , and the average KAM value was 0.41°. The formation of the deformed layer and ultrafine grains was attributed to the work hardening of the material. During the wear process, the dislocations in the grains proliferated and entangled under shear and compressive stresses, resulting in substructure refinement and an increase in the wear surface hardness.

The subsurface layer of the NbC-HEA sample also had an obvious TRIP effect after wear, and the thickness of the deformation layer with the TRIP effect was larger, that is, 50  $\mu\text{m}$  (Fig. 16a2). EBSD of the tensile fracture also showed a similar phenomenon. The NbC-HEA sample has a more significant TRIP effect than the C-HEA sample because the addition of Nb consumes C and reduces the SFE, which contributes to the TRIP effect. In addition, a small number of particles were partially exposed

outside the matrix, which hindered the interaction of the grinding ball, blocked the expansion of the groove, and increased the friction coefficient. At the same time, there was a certain height difference between the positions of the particles and the matrix without particles, which indicates that the existence of high-hardness particles can protect the matrix and reduce the wear rate. Fig. 16b2 clearly shows that there is an obvious grain refinement area in the wear subsurface layer. The grain size of the deformation layer structure marked in Fig. 16a2 was determined, and the grain size in this area was 0.71  $\mu\text{m}$ . The KAM distribution of the subsurface structure also indicates the existence of a deformation layer, but the thickness of the high-KAM area was still small, approximately 3.6  $\mu\text{m}$ , and the average KAM value was 0.48°.

By comparing the microstructure of the subsurface layers of the two alloys, the deformation layer of the subsurface layer of the NbC-HEA sample after wear was thicker, the HCP phase volume fraction generated by the phase transformation was higher, the average KAM value was higher, and the dislocation density increased with an increase in the KAM value, indicating that the NbC-HEA sample underwent more

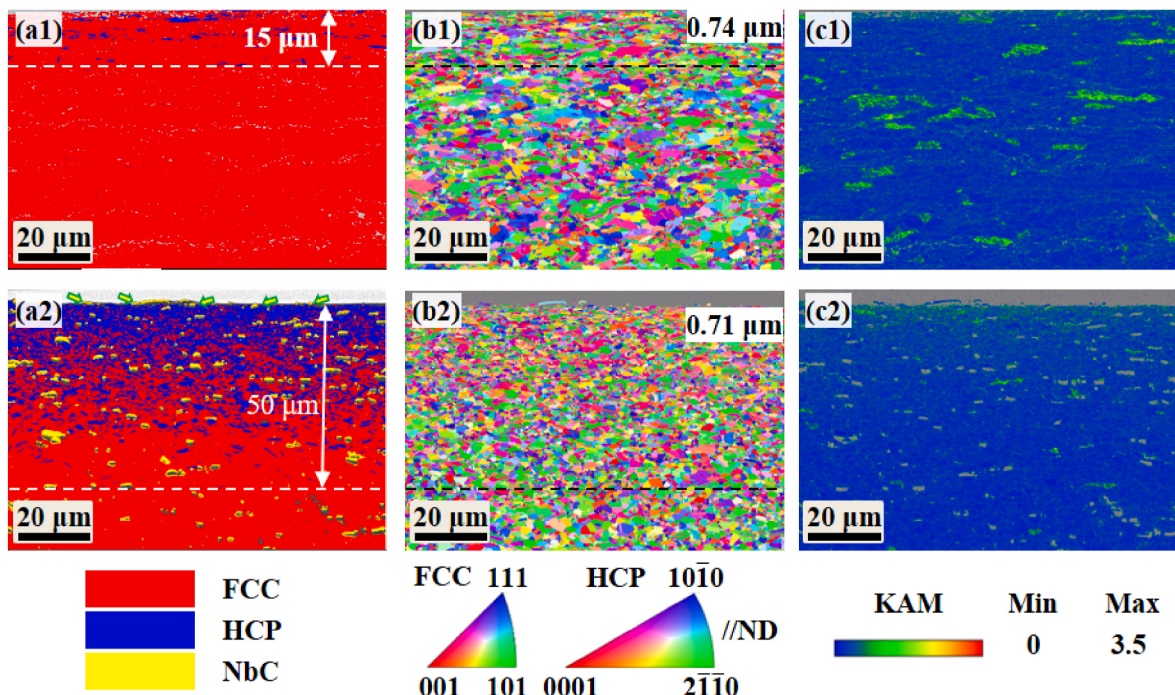


**Fig. 16.** The EBSD analysis results of the subsurface structure of the two alloys after wear at 30 N load: (a) phase distribution map; (b) IPF map; (c) KAM map; (1) C-HEA sample; (2) NbC-HEA sample.

significant processing during the wear process, which was also one of the reasons why the NbC-HEA sample had a lower wear rate.

As shown in the results calculated in the above analysis, the maximum contact stresses were 1.80, 2.27, and 2.60 GPa at loads of 10, 20, and 30 N, respectively. The tensile strength of the C-HEA sample was 995 MPa, and the tensile strength of the NbC-HEA sample was 937 MPa. The calculated stress was far more than the tensile strength of the material, indicating that the material has yielded. It was not an elastic Hertz contact, and the contact radius increased. At the same time, the maximum shear stress calculated according to the elastic Hertz contact model was 855, 1077, and 1232 MPa, respectively, while the shear yield strength of the two alloys was 317 MPa and 316 MPa, respectively, indicating that the shear force generated during the wear process was also much higher than the shear yield strength of the alloy. Therefore, under the load conditions selected in this paper, the material will cause severe wear and catastrophic damage. The wear rate was in the order of  $10^{-5} \text{ mm}^3/(\text{N}\cdot\text{m})$ , and this catastrophic damage will hardly occur in the actual working environment, otherwise the material will fail in a short time. The reason why this article uses large loads for experiments is that it will take a long time to get the results according to the actual situation, which is not conducive to scientific research. Therefore, the experiments carried out in the general laboratory are accelerated experiments. Similarly, the parameters selected in the standard of wear experiments and most wear-related papers can also cause catastrophic damage, which is also the need for accelerated experiments. In addition, many other experiments also use the method of accelerated test, such as high cycle fatigue test, which has been widely used as the standard of material fatigue performance. Although there are some differences in the wear mechanism and wear resistance of materials under low stress and high stress wear, the experimental results in this paper also prove this point, but it can still be used as a screening material with better wear resistance. At a load of 30 N, the wear rate of the NbC-HEA sample was 23.1 % lower than that of the C-HEA sample, but at a load of 10 N, the wear rate was reduced by 27.6 % indicating that the wear resistance of the NbC-HEA sample may be improved at lower loads. Because the stress applied in the experiment was high, there was a certain difference between the wear mechanism in the experiment and the wear mechanism

in the practical application process, and the accurate wear mechanism need to be analyzed by the materials in the practical application.

#### 4. Conclusion

The effects of Nb doping on the microstructure, mechanical properties, wear resistance, and deformation mechanism of the HEA Fe<sub>49</sub>Mn<sub>30</sub>Co<sub>10</sub>Cr<sub>10</sub>C<sub>1</sub> were studied by adding Nb at same atomic ratio of C. The results demonstrated that Nb doping produces multi-scale NbC particles with a volume fraction of about 2.3 %, while also maintaining yield strength and elongation and significantly reducing wear rate.

1. Nanoscale NbC will play a role in precipitation strengthening, but the formation of NbC will consume C atoms, reducing the role of interstitial strengthening. The two strengthening mechanism compete with each other, resulting in constant yield strength.
2. The formation of NbC consumes C atoms, reduces the SFE of the alloy, resulting in an increase in the volume fraction of the HCP phase in the tensile fracture from 13.2 % to 30.6 %, and offsets the deterioration effect of micron particles on elongation, keeping the elongation unchanged. During deformation, NbC particles pin the grain boundaries and dislocations, resulting in a decrease in the copper deformation texture intensity.
3. The wear mechanism of the two alloys in the sliding wear test were mainly abrasive wear, with the presence of NbC slightly increasing the friction coefficient. Nb doping reduced the SFE of the alloy, which caused it to form a thicker deformation layer and a strain-induced phase transition layer in the subsurface of the wear track. The thicker deformation layer and micron-sized NbC particles reduced the wear rate by more than 23.1 %.
4. The rationality of the existing method for calculating the wear rate with load as a parameter was analyzed, and a method for calculating the wear rate with maximum shear stress as a parameter was proposed. The advantage of this method was that it eliminated the influence of the physical characteristics of the material on the wear rate, making it more objective.

## CRediT authorship contribution statement

Qi Wang: Writing – original draft, Data curation, Formal analysis, Investigation. Yanjun Zhou: Writing – original draft, performed the TEM testing, Investigation. Xiangtao Deng: Writing – review & editing, Data curation, Formal analysis, Funding acquisition. Zhaodong Wang: Writing – review & editing, Data curation, Formal analysis, Funding acquisition.

## Declaration of competing interest

The authors declare that they have no known competing financial interests or personal relationships that could have appeared to influence the work reported in this paper.

## Data availability

Data will be made available on request.

## Acknowledgements

The authors acknowledge support from the National Basic Research Program, China (No. 2022YFB3705300), National Natural Science Foundation of China (No. 52274380, 51874089, U1960112), and LiaNing Revitalization Talents Program (No. XLYC2007030).

## References

- [1] W.Q. Hu, Z.Y. Huang, L.P. Cai, C. Lei, H.X. Zhai, Y. Zhou, Exploring the interfacial state and tensile behaviors in nickel matrix composite with in-situ TiC and  $\gamma$ -Ni<sub>3</sub>(Al,Ti) reinforcements, *J. Alloy. Compd.* 765 (2018) 987–993.
- [2] A.J. Zhang, J.S. Han, B. Su, J.H. Meng, A novel CoCrFeNi high entropy alloy matrix self-lubricating composite, *J. Alloys Compd.* 725 (2017) 700–710.
- [3] L. Huang, X.T. Deng, Y. Jia, C.R. Li, Z.D. Wang, Effects of using (Ti,Mo)C particles to reduce the three-body abrasive wear of a low alloy steel, *Wear* 410–411 (2018) 119–126.
- [4] Z.F. Li, Y.Q. He, G.M. Gao, J.J. Tang, X.J. Zhang, Z.Y. Liu, Effects of Al contents on microstructure and properties of hot-dip Zn-Al alloy coatings on hydrogen reduced hot-rolled steel without acid pickling, *J. Iron Steel Res. Int.* 24 (2017) 1032–1040.
- [5] F.M. Song, L.X. Du, Erosion corrosion of low-wear way-resistant steels in alkaline slurry, *J. Iron Steel Res. Int.* 24 (2017) 1065–1072.
- [6] Y. Yin, J.Q. Zhang, Q.Y. Tan, W. Zhuang, N. Mo, M. Bermingham, M.X. Zhang, Novel cost-effective Fe-based high entropy alloys with balanced strength and ductility, *Mater. Des.* 162 (2019) 24–33.
- [7] B. Gorr, M. Azim, H.J. Christ, T. Mueller, D. Schliephake, M. Heilmayer, Phase equilibria, microstructure, and high temperature oxidation resistance of novel refractory high-entropy alloys, *J. Alloys Compd.* 624 (2015) 270–278.
- [8] Z.F. He, N. Jia, H.W. Wang, H.L. Yan, Y.F. Shen, Synergy effect of multi-strengthening mechanisms in FeMnCoCrN HEA at cryogenic temperature, *J. Mater. Sci. Technol.* 86 (2021) 158–170.
- [9] Z.M. Li, C.C. Tasan, K.G. Pradeep, D. Raabe, A TRIP-assisted dual-phase high-entropy alloy: grain size and phase fraction effects on deformation behavior, *Acta Mater.* 131 (2017) 323–335.
- [10] M. Ghanbariha, M. Farvizi, T. Ebazdadeh, A. Alizadeh Samiyan, Effect of ZrO<sub>2</sub> particles on the nanomechanical properties and wear behavior of AlCoCrFeNi-ZrO<sub>2</sub> high entropy alloy composites, *Wear* 484–485 (2021), 204032.
- [11] Z.M. Guo, A.J. Zhang, J.S. Han, J.H. Meng, Microstructure, mechanical and tribological properties of CoCrFeNiMn high entropy alloy matrix composites with addition of Cr<sub>3</sub>C<sub>2</sub>, *Tribol. Int.* 151 (2020), 106436.
- [12] B.B. Xin, A.J. Zhang, J.S. Han, B. Su, J.H. Meng, Tuning composition and microstructure by doping Ti and C for enhancing mechanical property and wear resistance of Al<sub>0.2</sub>Co<sub>1.5</sub>Cr<sub>2</sub>Fe<sub>1.5</sub>Ti<sub>0.5</sub> high entropy alloy matrix composites, *J. Alloys Compd.* 836 (2020), 155273.
- [13] E. Abbasi, K. Dehghani, Effect of Nb-C addition on the microstructure and mechanical properties of CoCrFeMnNi high entropy alloys during homogenisation, *Mater. Sci. Eng., A* 753 (2019) 224–231.
- [14] J.F. Zhang, T. Jia, H. Qiu, H.G. Zhu, Z.H. Xie, Effect of cooling rate upon the microstructure and mechanical properties of in-situ TiC reinforced high entropy alloy CoCrFeNi, *J. Mater. Sci. Technol.* 42 (2020) 122–129.
- [15] M. Woydt, S. Huang, J. Vleugels, H. Mohrbacher, E. Cannizza, Potentials of niobium carbide (NbC) as cutting tools and for wear protection, *Int. J. Refract. Met. H.* 72 (2018) 380–387.
- [16] X.F. Li, Y.H. Feng, B.S. Liu, D.H. Yi, X.H. Yang, W.D. Zhang, G. Chen, Y. Liu, P. K. Bai, Influence of NbC particles on microstructure and mechanical properties of AlCoCrFeNi high-entropy alloy coatings prepared by laser cladding, *J. Alloys Compd.* 788 (2019) 485–494.
- [17] X.F. Li, X.H. Yang, D.H. Yi, B.S. Liu, J.C. Zhu, J.X. Li, C. Gao, L.Z. Wang, Effects of NbC content on microstructural evolution and mechanical properties of laser cladded Fe<sub>50</sub>Mn<sub>30</sub>Co<sub>10</sub>Cr<sub>10</sub>-xNbC composite coatings, *Intermetallics* 138 (2021), 107309.
- [18] X.W. Liu, N. Gao, J. Zheng, Y. Wu, Y.Y. Zhao, Q. Chen, W. Zhou, S.Z. Pu, W. M. Jiang, Z.T. Fan, Improving high-temperature mechanical properties of cast CrFeCoNi high-entropy alloy by highly thermostable in-situ precipitated carbides, *J. Mater. Sci. Technol.* 72 (2021) 29–38.
- [19] H. Chen, Y.N. Ma, C. Li, Q.Y. Zhao, Y.H. Huang, H. Luo, H.C. Ma, X.G. Li, A nano-sized NbC precipitation strengthened FeCoCrNi high entropy alloy with superior hydrogen embrittlement resistance, *Corrosion Sci.* 208 (2022), 110636.
- [20] E. Abbasi, K. Dehghani, Effect of Nb-C addition on the microstructure and mechanical properties of CoCrFeMnNi high entropy alloys during homogenisation, *Mater. Sci. Eng., A* 753 (2019) 224–231.
- [21] E. Abbasi, K. Dehghani, Hot tensile properties of CoCrFeMnNi(NbC) compositionally complex alloys, *Mater. Sci. Eng., A* 772 (2020), 138771.
- [22] Z. Zhang, Y.H. Xie, Y.X. Huo, S.L.I. Chan, J.M. Liang, Y.F. Luo, D.K.Q. Mu, J. Ju, J. Sun, J. Wang, Microstructure and mechanical properties of ultrafine grained CoCrFeNi and CoCrFeNiAl<sub>0.3</sub> high entropy alloys reinforced with Cr<sub>2</sub>O<sub>3</sub>/Al<sub>2</sub>O<sub>3</sub> nanoparticles, *Mater. Sci. Eng., A* 816 (2021), 141313.
- [23] C.R. Li, X.L. Li, X.T. Deng, Z.D. Wang, Revealing the role of micron-sized in situ TiC particles on tensile properties and fracture mechanism of martensitic wear-resistant steel at elevated temperature, *Mater. Sci. Eng., A* 832 (2022), 142503.
- [24] Y. Ikeda, I. Tanaka, J. Neugebauer, F. Körmann, Impact of interstitial C on phase stability and stacking-fault energy of the CrMnFeCoNi high-entropy alloy, *Phys. Rev. Mater.* 3 (2019), 113603.
- [25] K.Q. Yuan, Y. Jiang, S.C. Liu, S.S. Xu, X.Z. Li, X.X. Wu, Effect of carbon upon mechanical properties and deformation mechanisms of TWIP and TRIP-assisted high entropy alloys, *Mater. Sci. Eng., A* 857 (2022), 144126.
- [26] T.Z. Khan, T. Kirk, G. Vazquez, P. Singh, A.V. Smirnov, D.D. Johnson, K. Youssef, R. Arróyave, Towards stacking fault energy engineering in FCC high entropy alloys, *Acta Mater.* 224 (2022), 117472.
- [27] D.X. Wei, W. Gong, T. Tsuru, T. Kawasaki, S. Harjo, B. Cai, P.K. Liaw, H. Kato, Mechanical behaviors of equiatomic and near-equiatomic face-centered-cubic phase high-entropy alloys probed using in situ neutron diffraction, *Int. J. Plast.* 158 (2022), 103417.
- [28] X.X. Wei, X. Lin, W. Xu, Q.S. Huang, M. Ferry, J.F. Li, Y.H. Zhou, Remelting-induced anomalous eutectic formation during solidification of deeply undercooled eutectic alloy melts, *Acta Mater.* 95 (2015) 44–56.
- [29] W. Yu, M.L. Xin, Y. Li, T. Jiang, H.Y. Wang, Z.D. Wang, G.M. Xu, Tribological and texture analysis in Twin-roll casting 2060 Al-Li alloy, *Mater. Des.* 223 (2022), 111253.
- [30] C.H. Yin, Y.L. Liang, Y. Liang, W. Li, M. Yang, Formation of a self-lubricating layer by oxidation and solid-state amorphization of nano-lamellar microstructures during dry sliding wear tests, *Acta Mater.* 166 (2019) 208–220.
- [31] W.W. Zhu, C.C. Zhao, Y.W. Zhang, C.T. Kwok, J.H. Luan, Z.B. Jiao, F.Z. Ren, Achieving exceptional wear resistance in a compositionally complex alloy via tuning the interfacial structure and chemistry, *Acta Mater.* 188 (2020) 697–710.
- [32] Z. Cheng, L. Yang, Z.K. Huang, T. Wan, M.Y. Zhu, F.Z. Ren, Achieving low wear in a  $\mu$ -phase reinforced high-entropy alloy and associated subsurface microstructure evolution, *Wear* 474–475 (2021), 203755.
- [33] J. Joseph, N. Haghdadi, K. Shamlaye, P. Hodgson, M. Barnett, D. Fabijanic, The sliding wear behaviour of CoCrFeMnNi and AlxCrCoFeNi high entropy alloys at elevated temperatures, *Wear* 428–429 (2019) 32–44.
- [34] Y.S. Geng, W.Y. Chen, J. Cheng, J.J. Chen, S.Y. Zhu, J. Yang, W.M. Liu, Selective solid solution tailoring mechanical and tribological synergy in heterogeneous single-phase high-entropy alloys at elevated temperatures, *Tribol. Int.* 173 (2022), 107617.
- [35] H. Hertz, On the contact of rigid elastic solids, *J. Reine und Angewandte Mathematik* 92 (1882) 156–171.
- [36] G.M. Hamilton, L.E. Goodman, The stress field created by a circular sliding contact, *J. Appl. Mech.* 33 (1966) 371–376.
- [37] G.M. Hamilton, Explicit equations for the stresses beneath a sliding spherical contact, *P. I. Mech. Eng. C-J. Mec.* 197 (1983) 53–59.
- [38] J. Dutta Majumdar, B. Ramesh Chandra, I. Manna, Friction and wear behavior of laser composite surfaced aluminium with silicon carbide, *Wear* 262 (2007) 641–648.
- [39] J. Dutta Majumdar, B. Ramesh Chandra, I. Manna, Laser composite surfacing of AISI 304 stainless steel with titanium boride for improved wear resistance, *Tribol. Int.* 40 (2007) 146–152.
- [40] S.K. Karak, C.S. Vishnu, Z. Witczak, W. Lojkowski, J. Dutta Majumdar, I. Manna, Studies on wear behavior of nano-Y<sub>2</sub>O<sub>3</sub> dispersed ferritic steel developed by mechanical alloying and hot isostatic pressing, *Wear* 270 (2010) 5–11.
- [41] D. Roy, S.S. Singh, B. Basu, W. Lojkowski, R. Mitra, I. Manna, Studies on wear behavior of nano-intermetallic reinforced Al-base amorphous/nanocrystalline matrix in situ composite, *Wear* 266 (2009) 1113–1118.
- [42] L. Mujica Roncery, L. Agudo Jácome, A. Aghajani, W. Theisen, S. Weber, Subsurface characterization of high-strength high-interstitial austenitic steels after impact wear, *Wear* 402–403 (2018) 137–147.
- [43] V. Javaheri, S. Sadeghpour, P. Karjalainen, M. Lindroos, O. Haiko, N. Sarmadi, S. Pallaspuro, K. Valtonen, F. Pahlevani, A. Laukkanen, J. Kömi, Formation of nanostructured surface layer, the white layer, through solid particles impingement during slurry erosion in a martensitic medium-carbon steel, *Wear* 496–497 (2022), 204301.